

Cosmic Positron Signature from Dark Matter in the Littlest Higgs Model with T-parity

Masaki Asano^(a,b) ¹, Shigeki Matsumoto^(a) ², Nobuchika Okada^(a,b) ³,
and Yasuhiro Okada^(a,b) ⁴

^(a) *Theory Group, KEK, Oho 1-1 Tsukuba, 305-0801, Japan*

^(b) *The Graduate University for Advanced Studies (Sokendai),*

Oho 1-1 Tsukuba, 305-0801, Japan

Abstract

We calculate the flux of cosmic positrons from the dark matter annihilation in the littlest Higgs model with T-parity. The dark matter annihilates mainly into weak gauge bosons in the halo, and high energy positrons are produced through leptonic and hadronic decays of the bosons. We investigate a possibility to detect the positron signal in upcoming experiments such as PAMELA and AMS-02. We found that the dark matter signal can be distinguished from the background in the PAMELA experiment when the dark matter mass is less than 120 GeV and the signal flux is enhanced due to a small scale clustering of dark matter. Furthermore, the signal from the dark matter annihilation can be detected in the AMS-02 experiment, even if such enhancement does not exist. We also discuss the invisible width of the Higgs boson in this model.

¹E-mail: masano@post.kek.jp

²E-mail: smatsu@post.kek.jp

³E-mail: okadan@post.kek.jp

⁴E-mail: yasuihiro.okada@kek.jp

I Introduction

The hierarchy problem in the Standard Model (SM) is expected to give a clue to explore the physics beyond the SM. This problem is essentially related to quadratically divergent corrections to the Higgs boson mass, and we need a mechanism to avoid the divergences. To solve the problem, many scenarios have been proposed so far, for example supersymmetry, in which the divergences are completely removed. Other examples are scenarios with a low energy cutoff scale around a TeV such as Techni-color and TeV scale extra-dimension.

The latter scenarios are, however, constrained by the electroweak precision measurements. From the analysis of higher dimensional operators at the cutoff scale, it has been found that the scale should be larger than roughly 5 TeV [1]. For such high energy cutoff, the hierarchy problem appears again: We still need the fine-tuning of a few percent level in the Higgs mass term in order to obtain the 100-200 GeV Higgs boson mass. This problem is called the little hierarchy problem.

Recently the little Higgs model [2, 3] has been proposed for solving the little hierarchy problem. In this scenario, the Higgs boson is regarded as a pseudo Nambu-Goldstone boson. New particles such as heavy gauge bosons and a top-partner are introduced, and all quadratic divergences to the Higgs mass term completely vanish at one-loop level due to these particles' contributions. Thus, the fine-tuning of the Higgs boson mass is avoided even if the cutoff scale is around 10 TeV.

The original little Higgs model is still strongly constrained by the electroweak precision measurements [4]. This is mainly due to the contributions to electroweak observables from new heavy gauge bosons, because their masses are much smaller than the cutoff scale. In particular, direct couplings among a new heavy gauge boson and SM particles give sizable contributions to the observables. As a result, masses of new particles have to be raised, and the fine-tuning of the Higgs boson mass is reintroduced.

To resolve the problem, the implementation of the Z_2 symmetry called T-parity to the model has been proposed [5]-[7]. Under the parity, the new particles are assigned to be $-$ charge (T-odd), while the SM particles have $+$ charge (T-even). Thanks to the symmetry, dangerous interactions stated above are prohibited, and the masses of new particles can be lighter.

Due to the T-parity, the lightest T-odd particle becomes stable and a good candidate of the dark matter. This is an interesting feature of the model, because the

existence of the dark matter is now established by recent cosmological observations [8]. Since the lightest T-odd particle is electrically and color neutral, and has a mass of $\mathcal{O}(100)$ GeV [5] in many little Higgs models with T-parity, these models provide a WIMP (weakly interacting massive particle) dark matter [9], and are able to account for the large scale structure of the present universe [10].

In this paper, we study the dark matter phenomenology in the littlest Higgs model with T-parity [6, 7, 11]. The relic abundance of the dark matter in the thermal relic scenario has already been evaluated [11], and it has been found that the mass of the dark matter consistent with the WMAP observation [8] is around a few hundred GeV. In this paper, we focus on the indirect detection of this dark matter using the cosmic positrons. The dark matter in the halo associated with our galaxy frequently annihilates and produces high energy particles, for example, positrons [13]-[16], anti-protons [17], etc. Then high energy positron excess in the cosmic ray provides an opportunity to search for the dark matter signal.

In the littlest Higgs model with T-parity, the dark matter candidate is a heavy photon, which annihilates mainly into weak gauge bosons [11]. Positrons are produced through decays of the bosons. Since the dark matter annihilation occurs in the s-wave and weak gauge bosons can produce high energy positrons through leptonic decays, the resultant positron flux is large and its spectrum becomes harder than that of background positrons originating in a secondary production from cosmic protons. This feature is quite different from the spectrum of a bino-like neutralino dark matter in supersymmetric models, which is expected to be much softer. In this paper we calculate the positron flux from the dark matter annihilation in the model, and estimate the possibility to detect these positrons in future experiments such as PAMELA [18] and AMS-02 [19].

This paper is organized as follows. In the next section, we briefly review the littlest Higgs model with T-parity, in particular, focusing on the mass spectrum in the gauge-Higgs sector and interactions relevant to the calculation of the dark matter annihilation. We also present the thermal relic abundance of the dark matter. Calculation of the positron spectrum from the dark matter annihilation in the halo is performed in Sec.III using a diffusion model. Results of the positron flux are shown in Sec.IV. We also present the χ^2 -analysis in order to investigate a possibility to detect the positron signal in future experiments. Sec.V is devoted to summary and discussions including the Higgs decay into the dark matter. In Appendix, we consider constraints on the model from electroweak precision measurements, and

show that the entire region restricted by the WMAP observation can be consistent with the measurements.

II Dark Matter in Littlest Higgs Model with T-parity

We briefly review the littlest Higgs model with T-parity. In particular, we focus on the mass spectrum in the gauge-Higgs sector and interactions relevant to the dark matter in the model. We also calculate the relic abundance of the dark matter and present a parameter region of the model consistent with the WMAP observation [11]. For the general review of little Higgs models and some phenomenological aspects, see Refs[20, 21].

Littlest Higgs Model with T-parity

The littlest Higgs model [3] is based on a non-linear sigma model describing an SU(5)/SO(5) symmetry breaking. The non-linear sigma field Σ is given as

$$\Sigma = e^{2i\Pi/f}\Sigma_0 , \quad (1)$$

where f is the vacuum expectation value associated with the symmetry breaking. The Nambu-Goldstone boson matrix, Π , and the direction of the symmetry breaking in the non-linear field, Σ_0 , are written as

$$\Pi = \frac{1}{\sqrt{2}} \begin{pmatrix} 0 & H & \sqrt{2}\Phi \\ H^\dagger & 0 & H^T \\ \sqrt{2}\Phi^\dagger & H^* & 0 \end{pmatrix} , \quad \Sigma_0 = \begin{pmatrix} 0 & 0 & \mathbf{1} \\ 0 & 1 & 0 \\ \mathbf{1} & 0 & 0 \end{pmatrix} . \quad (2)$$

An $[\text{SU}(2) \times \text{U}(1)]^2$ subgroup in the global symmetry SU(5) is gauged, which is broken down to the diagonal subgroup identified with the SM gauge group $(\text{SU}(2)_L \times \text{U}(1)_Y)$. Due to the presence of the gauge interactions (and Yukawa interactions if we introduce), the global symmetry SU(5) is not exact, and the particles in the Π field become pseudo Nambu-Goldstone bosons.

Fourteen ($= 24 - 10$) Nambu-Goldstone bosons are decomposed into representations under the electroweak gauge group as $\mathbf{1}_0 \oplus \mathbf{3}_0 \oplus \mathbf{2}_{\pm 1/2} \oplus \mathbf{3}_{\pm 1}$. The first two representations are real, and become longitudinal components of gauge bosons when the $[\text{SU}(2) \times \text{U}(1)]^2$ is broken down to the SM gauge group. The representations $\mathbf{2}_{\pm 1/2}$ and $\mathbf{3}_{\pm 1}$ are a complex doublet identified with the SM Higgs field (H in Eq.(2)) and a complex triplet Higgs field (Φ in Eq.(2)), respectively.

The kinetic term for the Σ field is given as

$$\mathcal{L}_\Sigma = \frac{f^2}{8} \text{Tr} \left[D_\mu \Sigma (D^\mu \Sigma)^\dagger \right] , \quad (3)$$

where

$$D_\mu \Sigma = \partial_\mu \Sigma - i \sum_{j=1}^2 \left[g_j W_j^a (Q_j^a \Sigma + \Sigma Q_j^{aT}) + g'_j B_j (Y_j \Sigma + \Sigma Y_j) \right] . \quad (4)$$

Here, $W_j^a(B_j)$ are the $SU(2)_j(U(1)_j)$ gauge fields and $g_j(g'_j)$ are corresponding gauge coupling constants. The generators of the gauge symmetries Q_j and Y_j are

$$\begin{aligned} Q_1^a &= \frac{1}{2} \begin{pmatrix} \sigma^a & 0 & 0 \\ 0 & 0 & 0 \\ 0 & 0 & 0 \end{pmatrix} , & Y_1 &= \text{diag}(3, 3, -2, -2, -2)/10 , \\ Q_2^a &= -\frac{1}{2} \begin{pmatrix} 0 & 0 & 0 \\ 0 & 0 & 0 \\ 0 & 0 & \sigma^{a*} \end{pmatrix} , & Y_2 &= \text{diag}(2, 2, 2, -3, -3)/10 , \end{aligned} \quad (5)$$

where σ^a are the Pauli matrices.

In terms of above fields, the symmetry of the T-parity [5]-[7] is defined as the invariance of the Lagrangian under the transformation:

$$W_1^a \leftrightarrow W_2^a , \quad B_1 \leftrightarrow B_2 , \quad \Pi \leftrightarrow -\Omega \Pi \Omega , \quad (6)$$

where $\Omega = \text{diag}(1, 1, -1, 1, 1)$. As a result of the symmetry, the gauge coupling $g_1(g'_1)$ must be equal to $g_2(g'_2)$, namely $g_1 = g_2 = \sqrt{2}g$ ($g'_1 = g'_2 = \sqrt{2}g'$), where $g(g')$ is nothing but the coupling constant of the SM $SU(2)_L(U(1)_Y)$ gauge symmetry.

Since the Higgs boson is the pseudo Nambu-Goldstone boson, its potential is generated radiatively [3, 11]

$$V(H, \Phi) = \lambda f^2 \text{Tr} \left[\Phi^\dagger \Phi \right] - \mu^2 H^\dagger H + \frac{\lambda}{4} (H^\dagger H)^2 + \dots . \quad (7)$$

Due to the little Higgs mechanism, quadratic divergent corrections do not contribute to the Higgs mass μ^2 at 1-loop level, while the corrections do contribute to the triplet Higgs mass term. Main contributions to μ^2 come from the logarithmic divergent corrections at 1-loop level and quadratic divergent corrections at 2-loop level. As a result, μ^2 is expected to be smaller than f^2 , while the triplet Higgs mass term is proportional to f^2 . The quartet coupling λ is determined by the 1-loop effective

potential from gauge and top sectors. Since both μ and λ depend on parameters at the cutoff scale, we treat these as free parameters in this paper.

We discuss the mass spectrum of gauge and Higgs bosons. This model contains four kinds of gauge fields W_1^a , W_2^a , B_1 and B_2 in the electroweak gauge sector. The combinations, $W^a = (W_1^a + W_2^a)/\sqrt{2}$ and $B = (B_1 + B_2)/\sqrt{2}$, correspond to the SM gauge bosons for the $SU(2)_L$ and $U(1)_Y$ symmetry. The other combinations, $W_H^a = (W_1^a - W_2^a)/\sqrt{2}$ and $B_H = (B_1 - B_2)/\sqrt{2}$, are additional gauge bosons, which acquire the masses of $\mathcal{O}(f)$ through the $SU(5)/SO(5)$ symmetry breaking. After electroweak symmetry breaking, neutral components of W_H^a and B_H are mixed and form mass eigenstates A_H and Z_H . The masses of the heavy bosons are obtained as

$$\begin{aligned} m_{Z_H} &= \frac{1}{2} \left(A + C + \sqrt{(A - C)^2 + 4B^2} \right) \simeq gf, \\ m_{A_H} &= \frac{1}{2} \left(A + C - \sqrt{(A - C)^2 + 4B^2} \right) \simeq \frac{g'}{\sqrt{5}}f, \end{aligned} \quad (8)$$

where $A = g^2(f^2 - v^2/4)$, $B = gg'v^2/4$ and $C = g'^2(f^2/5 - v^2/4)$. The mixing angle between W_H^a and B_H are given as

$$\tan \theta_H = -\frac{2B}{A - C + \sqrt{(A - C)^2 + 4B^2}} \simeq -\frac{gg'v^2}{4f^2(g^2 - g'^2/5)}, \quad (9)$$

which is suppressed by $\mathcal{O}(v/f)$. In addition to these gauge fields, we have the triplet Higgs boson Φ in this model, and its mass is given by $m_\Phi^2 = \lambda f^2 = 2m_h^2 f^2/v^2$, where m_h is the mass of the SM Higgs boson and v ($\simeq 246$ GeV) is the vacuum expectation value of the Higgs field. New heavy gauge bosons and the triplet Higgs boson are T-odd particles, while SM particles are T-even.

The mass spectrum of T-odd particles are determined by two parameters, the breaking scale (f) and the Higgs boson mass (m_h). For instance, in the case of $m_h = 120$ GeV and $f = 700$ GeV, $m_{A_H} = 100$ GeV, $m_{W_H(Z_H)} = 450$ GeV and $m_\Phi = 500$ GeV. As shown in Eq.(8), the mass of the heavy photon is considerably lighter than other T-odd particles due to the small hypercharge. Thus its stability is guaranteed by the T-parity conservation and becomes a candidate of a non-baryonic cold dark matter.

In addition to these new particles, top-partners are introduced in this model in order to cancel the quadratic divergent contribution to the Higgs mass term from the top quark loop diagrams. Due to the T-parity, three kinds of partners exist, namely T-even heavy top (T_+) which is introduced for the cancellation, T-partners of heavy top and top quark (T_- and t_-). The mass spectrum of these particles depends not

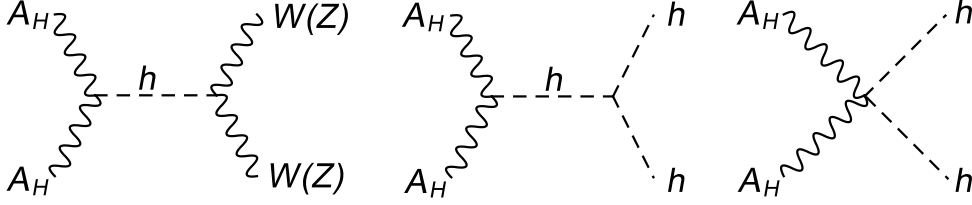


Figure 1: Feynman diagrams for the annihilation of the dark matter (A_H).

only on f and m_h , but also on other model parameters. Since these particles do not play a significant role in the dark matter phenomenology, we do not discuss this sector here.

Relic Abundance of Dark Matter

The dark matter (A_H) in the model annihilates mainly into weak gauge bosons, W^+W^- , ZZ through the diagrams in which the Higgs boson propagates in the s-channel. The dark matter also annihilates into Higgs bosons if $m_{A_H} > m_h$. The Feynman diagrams for these processes are shown in Fig.1¹. From Eqs.(3) and (7), interactions relevant to the annihilation are given as

$$\mathcal{L}_{\text{int}} = c \left(v h + \frac{h^2}{2} \right) A_H^2 + \frac{g^2 v}{2} h W^+ W^- + \frac{(g^2 + g'^2) v}{4} h Z^2 - \frac{m_h^2}{2v} h^3, \quad (10)$$

where $c = -(g \sin \theta_H - g' \cos \theta_H)^2 / 4$. We have used the unitary gauge $H = (0, v + h)^T / \sqrt{2}$. From the interactions, the annihilation cross sections of the dark matter turn out to be

$$\begin{aligned} \sigma v|_{WW} &= \frac{1}{96\pi m_{A_H}^2} \frac{(g^2 v^2 c)^2}{(4m_{A_H}^2 - m_h^2)^2 + m_h^2 \Gamma_h^2} \left(4 \frac{m_{A_H}^4}{m_W^4} - 4 \frac{m_{A_H}^2}{m_W^2} + 3 \right) \sqrt{1 - \frac{m_W^2}{m_{A_H}^2}}, \\ \sigma v|_{ZZ} &= \frac{1}{192\pi m_{A_H}^2} \frac{[(g^2 + g'^2) v^2 c]^2}{(4m_{A_H}^2 - m_h^2)^2 + m_h^2 \Gamma_h^2} \left(4 \frac{m_{A_H}^4}{m_Z^4} - 4 \frac{m_{A_H}^2}{m_Z^2} + 3 \right) \sqrt{1 - \frac{m_Z^2}{m_{A_H}^2}}, \\ \sigma v|_{hh} &= \frac{c^2}{48\pi m_{A_H}^2} \left| 1 + \frac{3m_h^2}{4m_{A_H}^2 - m_h^2 + im_h \Gamma_h} \right|^2 \sqrt{1 - \frac{m_h^2}{m_{A_H}^2}}, \end{aligned} \quad (11)$$

¹There are also diagrams in which the T-partners of fermions are exchanged in the t-channel. These contributions are, however, negligible compared to those in Fig.1 unless masses of T-partners are much smaller than 1 TeV. In fact, as discussed in Ref.[22], the cross sections for these processes are suppressed by masses of the T-partners, $m_{f_H}^4$, and small hypercharges, $\tilde{Y}^4 = (0.1)^4$.

where v is the relative velocity between incident dark matters, and Γ_h is the width of the SM Higgs boson. We take the non-relativistic limit ($v \rightarrow 0$) in the calculation, because the dark matter is almost at rest at the freeze-out temperature.

The relic abundance of the dark matter is obtained by solving the following Boltzmann equation [23],

$$\frac{dY}{dx} = -\frac{\langle\sigma v\rangle}{Hx} s (Y^2 - Y_{\text{eq}}^2) , \quad (12)$$

where $Y = n/s$ is the yield of the dark matter defined by the ratio of the dark matter density (n) to the entropy density of the universe ($s = 0.439g_*m_{A_H}^3/x^3$), $g_* = 86.25$ and $x \equiv m_{A_H}/T$ (T is the temperature of the universe). The Hubble parameter is given by $H = 1.66g_*^{1/2}m_{A_H}^2m_{\text{Pl}}/x^2$, where $m_{\text{Pl}} = 1.22 \times 10^{19}$ GeV is the Planck mass. The yield in the equilibrium Y_{eq} is written as

$$Y_{\text{eq}} = \frac{45}{2\pi^4} \left(\frac{\pi}{8}\right)^{1/2} \frac{3}{g_*} x^{3/2} e^{-x} . \quad (13)$$

Since the dark matter annihilates into the SM particles in the s-wave at the non-relativistic limit, the thermal averaged annihilation cross section ($\langle\sigma v\rangle$) is simply given by

$$\langle\sigma v\rangle = \sigma v|_{WW} + \sigma v|_{ZZ} + \sigma v|_{hh} , \quad (14)$$

After solving the Boltzmann equation, we obtain the present abundance of dark matter (Y_∞). It is useful to express the relic density in terms of the ratio of the dark matter density to the critical density ($\Omega h^2 = m_{A_H} n h^2 / \rho_c = m_{A_H} s_0 Y_\infty h^2 / \rho_c$), where $\rho_c = 1.1 \times 10^{-5} h^2 \text{ cm}^{-3}$, $h = 0.71_{-0.03}^{+0.04}$ and $s_0 = 2900 \text{ cm}^{-3}$. With a good accuracy, the solution of Eq.(12) is approximately given as

$$\Omega h^2 = \frac{1.07 \times 10^9 x_f \text{ GeV}^{-1}}{\sqrt{g_*} m_{\text{PL}} \langle\sigma v\rangle} , \quad (15)$$

where $x_f = m_{A_H}/T_f$ is the freeze-out temperature for the dark matter and given as $x_f = \ln(X) - 0.5 \ln(\ln(X))$ with $X = 0.038 \cdot (3/g_*^{1/2}) m_{\text{PL}} m_{A_H} \langle\sigma v\rangle$. Typically x_f takes a value, $x_f \simeq 23$.

The relic abundance of the dark matter in the thermal scenario is depicted in Fig.2 as a contour map in the (f, m_h) -plane. The shaded thin area is the allowed region for the WMAP observation at 2σ level, $0.094 < \Omega h^2 < 0.129$ [8]. The result obtained here is consistent with the previous calculation in Ref.[11]. As shown in the figure, the breaking scale f is constrained to be less than about 2 TeV.

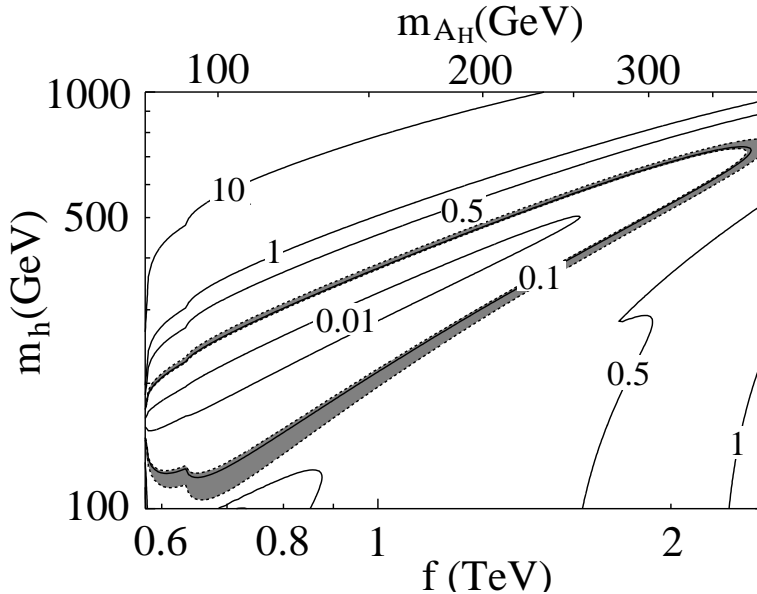


Figure 2: Contour plot of the thermal relic abundance for the dark matter (Ωh^2) in the (f, m_h) -plane. The shaded thin area is the allowed region from the WMAP observation at 2σ level, $0.094 < \Omega h^2 < 0.129$.

The lightest Higgs model with T-parity is constrained from the electroweak precision measurements. New physics contributions to the electroweak observables come from radiative corrections, because there is no tree-level effect due to the T-parity. As a result, the constraint to the model becomes weaker than that for the model without T-parity. The detailed analysis has been performed in Ref.[12]. We have repeated this analysis and present the result in Appendix. It is shown that the entire region is consistent with the electroweak precision measurements by choosing parameters in the top sector.

III Propagation of Positron from Dark Matter Annihilation in Galaxy

In the present universe, a dark matter makes up a halo associated with a galaxy. The distribution of the dark matter in the halo is given from a halo mass profile $\rho(\vec{r})$ through the equation $n(\vec{r}) = \rho(\vec{r})/m$. The profile is determined by observations of the rotational velocity of the galaxy and the motions of the dwarf galaxies with help of N-body simulations. Several models for the profile have been proposed [24]. For

our galaxy, we use the isothermal halo model in this paper, which is given as

$$\rho(\vec{r}) = \rho_0 \frac{1 + r_0^2/r_c^2}{1 + r^2/r_c^2} \text{ (GeV/cm}^3\text{)} , \quad (16)$$

where $r = |\vec{r}|$ is the distance from the galactic center, $\rho_0 \simeq 0.43 \text{ GeV/cm}^3$ is the local halo density in the vicinity of the solar system, $r_c \simeq 2.8 \text{ kpc}$ is the core radius of the galaxy, and $r_0 \simeq 8.5 \text{ kpc}$ is the distance between the galactic center and the solar system.

In an indirect detection of dark matter, high energy particles from the dark matter annihilation are expected to be observed in the cosmic ray. Several kinds of annihilation products are produced, among which we focus on positrons [13]. We calculate the expected flux of the positrons at the earth from the annihilation. In evaluation of the flux, we need to take into account the propagation of positrons through the galaxy. We also address the background positrons originated from the secondary production of the cosmic ray.

Production Rate of Positrons from Dark Matter Annihilation

The dark matter annihilates mainly into weak gauge bosons and the Higgs bosons as discussed in the previous section. Positrons are produced through leptonic and hadronic cascade decays of these bosons. For W bosons, these processes are $W^+ \rightarrow e^+\nu$, $W^+ \rightarrow \mu^+\nu \rightarrow e^+\nu\bar{\nu}$ or $W^\pm \rightarrow \text{hadrons} \rightarrow \pi^\pm \rightarrow \mu^\pm \rightarrow e^\pm$. Decay branching ratio for the Higgs boson depends on its mass. When $m_h > 160 \text{ GeV}$, the Higgs boson mainly decays into weak gauge bosons, and positrons are produced by decays of weak bosons.

Using the annihilation cross sections in Eq.(11), the production rate of positrons from the annihilation is given as

$$Q(E, \vec{r}) = \frac{1}{2} n^2(\vec{r}) \sum_{f=WW,ZZ,hh} (\sigma_{fv}) \left(\frac{dN_{e^+}}{dE} \right)_f , \quad (17)$$

where E is the energy of a positron and the coefficient $1/2$ comes from the pair annihilation of the identical particles. The fragmentation function $(dN_{e^+}/dE)_f$ represents the number of positrons with energy E produced from the final state f . The cascade processes for the positron production discussed above are encoded into these functions.

The fragmentation functions are evaluated by a Monte-Carlo simulation such as the HERWIG code [25]. These functions for the weak gauge bosons can be parame-

terized by a single variable $x = E/m$. The fitting functions have been constructed in Ref.[26] to reproduce results of the simulation. We use these functions in this paper. The fragmentation function for the Higgs boson is also obtained by assuming the dominance of gauge boson decay modes.

Although we use the isothermal model in Eq.(16), the high energy positron flux does not strongly depend on the choice of dark matter halo models. Main difference among proposed models appears in the region around the galactic center, and positrons produced around this region can not reach the earth without the significant energy loss.

Recently, the effect of inhomogeneity in the local dark matter distribution on the positron flux is discussed based on the N-body simulations. It is shown that the positron flux from the dark matter annihilation is enhanced if there are clumps of the dark matter in the vicinity of the solar system [27]. The effect is parameterized as a boost factor (BF), which is defined by the ratio of the signal fluxes with inhomogeneity and without inhomogeneity,

$$BF = \frac{V \int_V d^3x \rho^2}{\left(\int_V d^3x \rho \right)^2}, \quad (18)$$

where the region of the integration is taken to be $V \sim (\text{a few kpc})^3$ around the solar system. The boost factor is larger than 1, and equal to 1 only if the density ρ is a constant. The value of the factor is expected to be in the range of 2 to 5 based on a hierarchical clustering scenario in the inflationary universe [28].

Positron Propagation in Galaxy

Once positrons are produced in the dark matter annihilation, they travel in our galaxy under the influence of a tangled magnetic field. Since the typical strength of the magnetic field is a micro Gauss, the gyro-radius of the positron is much less than the galactic radius. Thus, the propagation can be treated as a random walk.

We use a diffusion model for the propagation of positrons, in which the random walk is described by the following diffusion equation [15, 26],

$$\frac{\partial}{\partial t} f_{e^+}(E, \vec{r}) = K(E) \nabla^2 f_{e^+}(E, \vec{r}) + \frac{\partial}{\partial E} [b(E) f_{e^+}(E, \vec{r})] + Q(E, \vec{r}), \quad (19)$$

where $f_{e^+}(E, \vec{r})$ is the number density of positrons per unit energy, E is the energy of positron, $K(E)$ is the diffusion constant, $b(E)$ is the energy loss rate, and $Q(E, \vec{r})$

is the source (positron injection) term discussed in the previous subsection. The flux of positrons with high energy ($E \gg m_e$) in the vicinity of the solar system is given from $f_{e^+}(E, \vec{r})$ as

$$\Phi_{e^+}(E) = BF \frac{1}{4\pi} f_{e^+}(E, \vec{r}_\odot) , \quad (20)$$

where \vec{r}_\odot represents the coordinate of the solar system.

There are two parameters in Eq.(19). One is the diffusion constant $K(E)$ characterizing the tangled magnetic field of the galaxy. This parameter is evaluated by comparing the observations of the Boron to Carbon ratio in the cosmic ray with the result of simulations [29]. The parameter $b(E)$ stands for the energy loss rate of positrons due to the inverse Compton scattering with cosmic microwave radiation (and infrared photons from stars) and synchrotron radiation with the magnetic field during the propagation in the galaxy [30]. This parameter is, therefore, determined by the photon density, the strength of the magnetic field and the Thomson scattering cross section. For both parameters, we use values adopted in Ref.[15]

$$\begin{aligned} K(E) &= 3.3 \times 10^{27} [3^{0.6} + (E/1 \text{ GeV})^{0.6}] \text{ (cm}^2\text{s}^{-1}) , \\ b(E) &= 10^{-16} (E/1 \text{ GeV})^2 \text{ (GeV s}^{-1}) . \end{aligned} \quad (21)$$

The positrons from the dark matter annihilation are expected to be in the equilibrium in our galaxy, hence the number density $f_{e^+}(E, \vec{r})$ is obtained by solving Eq. (19) with the steady state condition $\partial f_{e^+}/\partial t = 0$. Furthermore, we impose the free escape boundary condition, namely the positron density drops to zero on the surface of the diffusion zone. This means that the positrons coming from the outside of the zone are negligible, while the positrons produced inside the zone contribute to the flux around the solar system due to the trapping by the tangled magnetic field [31]. The diffusion zone is usually assumed to be a cylinder with the half-height (L) and radius (R), which are set to be $L = 4$ kpc and $R = 20$ kpc in this paper.

The high energy positron flux at the earth does not strongly depend on the choice of the diffusion zone, because the positrons we observe are produced within a few kpc around the solar system. In fact, the distance in which positrons travel without significant energy loss is estimated as $r \sim \sqrt{EK(E)/b(E)} \sim 0.74 \times (E/100 \text{ GeV})^{-0.2}$ kpc. Positrons far from the earth lose their energies during the propagation, and consequently they only contribute to the low-energy part of the flux.

The flux obtained from Eq.(20) does not correspond exactly to the one observed on the top of atmosphere. The flux is modified due to interaction with the solar

wind and the magneto-sphere [32]. However, the modulation effect is not important when the energy of a positron is above 10 GeV. Furthermore, the effect is highly suppressed in the positron fraction, which is defined by a ratio of the positron flux to the sum of positron and electron fluxes, *i.e.* $\Phi_{e^+}/(\Phi_{e^+} + \Phi_{e^-})$.

Background Positrons

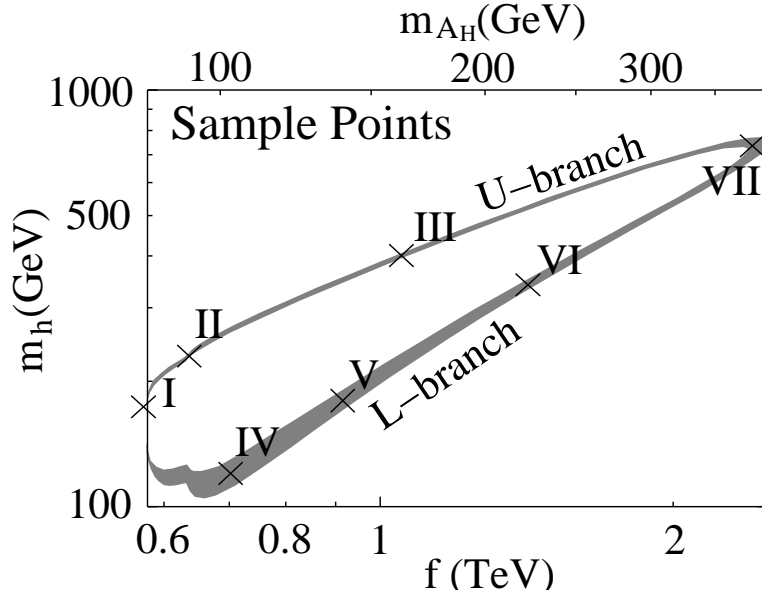
In the detection of the positrons from the dark matter annihilation, the main background comes from high energy positrons in the cosmic ray. High energy positrons are produced as secondary particles in the collision between hydrogen and helium in interstellar medium and primary particles in cosmic ray accelerated by the shock wave in supernovas. The flux of these positrons are obtained by simulations, in which a diffusion model is also used. The result of simulations agrees with measurements of the low-energy positron flux in the cosmic ray [33]. The fitting functions for high energy positrons, primary electrons, and secondary electrons have been constructed [15],

$$\begin{aligned}
\Phi_{e^-}^{(\text{prim})}(E) &= \frac{0.16E^{-1.1}}{1 + 11E^{0.9} + 3.2E^{2.15}} \text{ (GeV}^{-1}\text{cm}^{-2}\text{s}^{-1}\text{sr}^{-1}\text{)} , \\
\Phi_{e^-}^{(\text{sec})}(E) &= \frac{0.70E^{0.7}}{1 + 110E^{1.5} + 600E^{2.9} + 580E^{4.2}} \text{ (GeV}^{-1}\text{cm}^{-2}\text{s}^{-1}\text{sr}^{-1}\text{)} , \\
\Phi_{e^+}^{(\text{sec})}(E) &= \frac{4.5E^{0.7}}{1 + 650E^{2.3} + 1500E^{4.2}} \text{ (GeV}^{-1}\text{cm}^{-2}\text{s}^{-1}\text{sr}^{-1}\text{)} , \tag{22}
\end{aligned}$$

where E is in unit of GeV. The first one, $\Phi_{e^-}^{(\text{prim})}$, is the flux of the primary electrons, while the second and third ones, $\Phi_{e^-}^{(\text{sec})}$ and $\Phi_{e^+}^{(\text{sec})}$, are the secondary electron and positron fluxes, respectively.

IV Positron Signal from Dark Matter Annihilation in Halo

We are now in position to discuss the positron signal from the dark matter annihilation. The signal positron flux is evaluated in Eq.(20), while expected positron and electron background are given in Eqs.(22). In order to show how the dark matter annihilation can modify the positron energy spectrum in the cosmic ray, we have chosen seven sample-points (I to VII) in the parameter space of the little Higgs model with T-parity as in Fig.3. Parameters f and m_h and masses of various particles are



(GeV unit)	I	II	III	IV	V	VI	VII
f	577	637	1050	702	916	1418	2470
m_h	170	230	400	120	180	340	740
m_{A_H}	80.3	91.2	162	103	139	222	392
$m_{W_H}(m_{Z_H})$	367	406	678	450	590	919	1600
m_Φ	564	842	2410	484	948	2770	10500

Figure 3: Sample-points for depicting the positron fraction from the dark matter annihilation. The shaded thin area is the allowed region from the WMAP observation at 2σ level. In the table below the figure, the details about model parameters in each point are shown.

listed in the table below the figure. All points satisfy the WMAP condition, namely the present dark matter abundance is explained by the thermal relic scenario. As seen in the figure, there are two branches: the upper branch (U-branch) and lower branch (L-branch). In the U-branch, the Higgs boson mass is larger than twice the dark matter mass, $m_h > 2m_{A_H}$, while $m_h < 2m_{A_H}$ in the L-branch.

In Fig.4, the positron fraction, $\Phi_{e^+}/(\Phi_{e^+}+\Phi_{e^-})$, is shown as a function of positron energy. In the left figure, the results for the points in the U-branch (I to III) are depicted, while those in the L-branch (IV to VI) are in the right figure. The point VII can be regarded as a sample on both U- and L-branches, and its result are shown in both figures. We used the boost factor $BF = 5$. The expected background positron

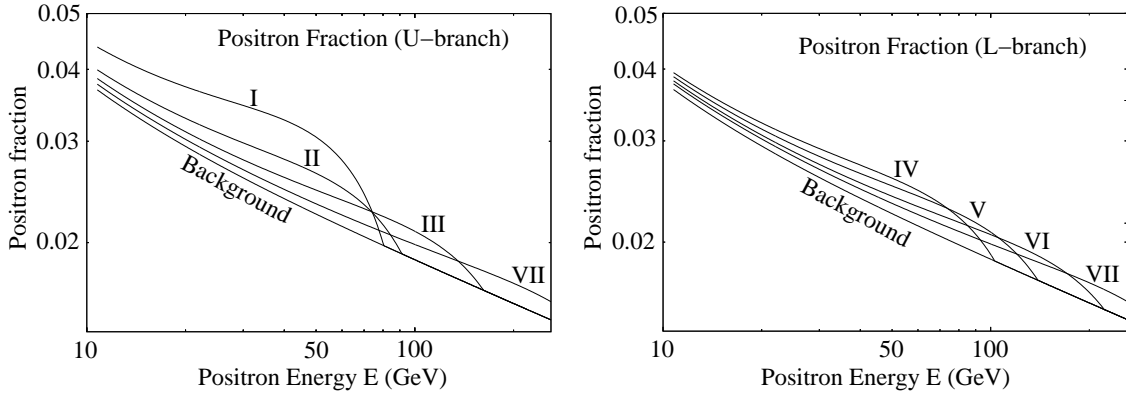


Figure 4: The positron fraction as a function of positron energy E . For comparison, the expected background fraction is also shown in these figures. In the left figure, the fraction in the U-branch (I to III and VII) are depicted, while those in the L-branch (IV to VI and VII) are in the right figure. In both figures, the boost factor $BF = 5$ is used.

fraction is also shown for comparison.

The upcoming experiments such as PAMELA and AMS-02 have good sensitivities in a broad range for a positron energy $10 \text{ GeV} \leq E \leq 270 \text{ GeV}$. In order to discuss the possibility for detection of the dark matter signal in the future experiments, we perform the χ^2 -analysis developed in Ref.[16]. For this purpose, we need to know the expected signal and background events in future experiments for each parameter point of the model (f, m_h) . The χ^2 is defined as

$$\chi^2 = \sum_i \frac{(N_i^{(\text{Obs})} - N_i^{(\text{BG})})^2}{N_i^{(\text{Obs})}} , \quad (23)$$

where the sum is taken over energy bins, $N_i^{(\text{Obs})}$ is the number of positron events observed in the i -th bin and $N_i^{(\text{BG})}$ is the number of events expected from the background contribution in the bin. Following the Ref.[16], we chose 22 bins in the range between $10 \text{ GeV} < E < 270 \text{ GeV}$,

$$\begin{aligned} \Delta[\log_{10}(E/1\text{GeV})] &= 0.06 , & (E \leq 40\text{GeV}) , \\ \Delta[\log_{10}(E/1\text{GeV})] &= 0.066 , & (E > 40\text{GeV}) . \end{aligned} \quad (24)$$

In our analysis, we use the acceptance of PAMELA and AMS-02 to be $20.5\text{cm}^2\text{sr}$ and $450\text{cm}^2\text{sr}$, respectively, assuming three years of data-taking.

In Fig.5, the contour plot of the χ^2 is depicted in (f, m_h) -plane. The left figure is the χ^2 in the PAMELA experiment with $BF = 5$, while the right one is the χ^2

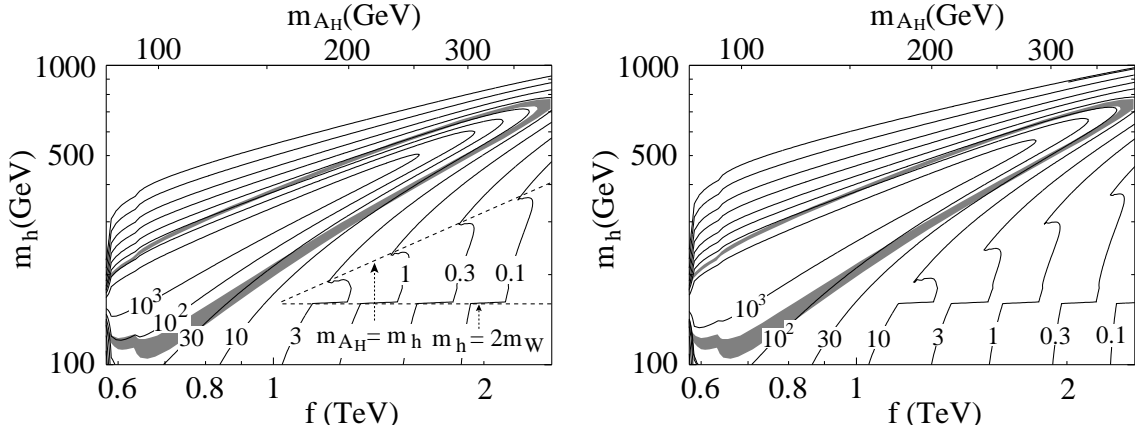


Figure 5: The contour plot of the χ^2 in (f, m_h) -plane. The left figure is the χ^2 in the PAMELA experiment with $BF = 5$, while the right one is the χ^2 in the AMS-02 with $BF = 2$. For comparison, the constraint from the WMAP observation is also shown as a shaded region. The values of χ^2 , 30.8, 33.9 and 40.3, correspond to the statistical significance for the detection of the signal at the 90%, 95% and 99% confidence levels.

in the AMS-02 with $BF = 2$.² The statistical significance for the detection of the signal at the 90%, 95% and 99% confidence levels correspond to the values of χ^2 , 30.8, 33.9 and 40.3. In these figures, the constraint from the WMAP observation is also shown as a shaded region. Inside the region, predicted thermal relics of the dark matter are smaller, while the relics outside the region are larger than that observed in the WMAP observation. If we like to consider parameter region inconsistent with the WMAP observation, deviation from the thermal relic scenario is necessary such as a non-thermal production of dark matter or entropy production at late time.

The strange behavior around $f > 1$ TeV and $m_h \sim 200$ -400 GeV in the figures is due to the annihilation mode into two Higgs bosons. When this annihilation channel is opened ($m_{A_H} > m_h$) and the Higgs boson mass is larger than twice the W boson mass ($m_H > 2m_W$), high energy positrons are produced through the process $A_H A_H \rightarrow hh \rightarrow WWWW$. These positrons have a hard spectrum, and enhance the possibility to detect the dark matter signal. On the other hand, when the Higgs boson mass is less than that of two W bosons ($m_H < 2m_W$), the effect becomes negligible. Since positrons are produced through cascade decays of b-quarks, the resultant spectrum in the process becomes very soft.

²The value of χ^2 is proportional to BF^2 , thus the extension of the result in other values of the boost factor is straightforward.

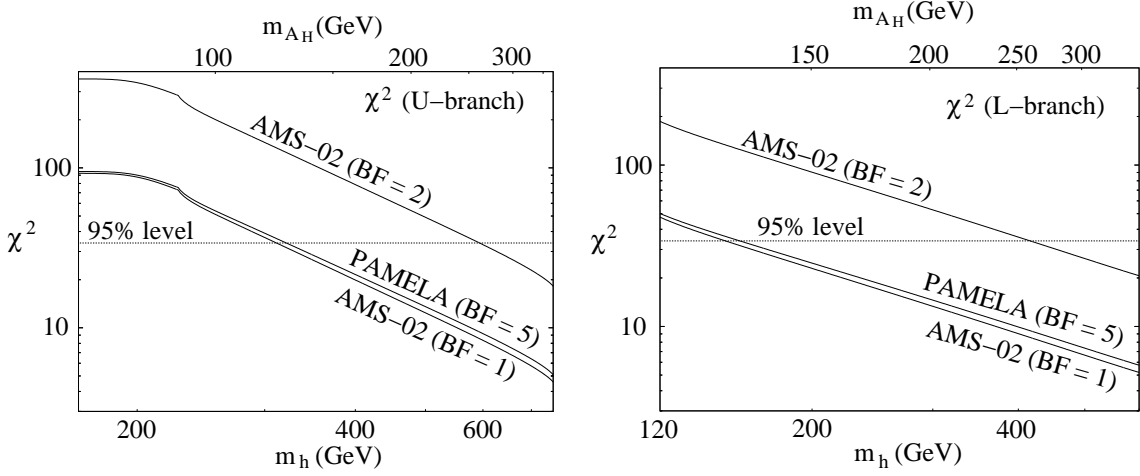


Figure 6: χ^2 plot along the center value ($\Omega h^2 = 0.112$) of U- (left figure) and L-branch (right figure) as a function of the Higgs boson mass m_h and the dark matter mass m_{A_H} (see the top axis). In both figures, the χ^2 of PAMELA with $BF = 5$, AMS-02 with $BF = 2$, and $BF = 1$ are depicted.

From the left figure, we see that the dark matter signal is clearly distinguished from the background in the PAMELA experiment when the breaking scale f is less than 1 TeV for $BF = 5$. On the other hand, from the right figure, almost all interesting area including the WMAP region is covered in AMS-02 with $BF = 2$. Furthermore, the value of χ^2 in the AMS-02 with $BF = 1$ is quite similar to the plot in the PAMELA with $BF = 5$. Thus it is possible to detect the signal in AMS-02 even if there is no enhancement from the boost factor.

The χ^2 plot along the center value ($\Omega h^2 = 0.112$) of U- and L-branch as a function of the Higgs boson mass m_h and dark matter mass m_{A_H} are presented in Fig.6. The result of the U-branch case is shown in the left figure, while that of the L-branch is in the right figure. In both figures, the χ^2 of the PAMELA with $BF = 5$, AMS-02 with $BF = 2$ and $BF = 1$ are depicted. For the reference, the line $\chi^2 = 33.9$ (corresponds to the 95% confidence level) is shown. The decreasing behavior of χ^2 along with increasing m_h is due to the fact that a number density of the dark matter is decreasing as m_{A_H} is increasing. If the boost factor is around 5, the PAMELA experiment has a potential to detect the dark matter signal when $m_h < 300$ GeV ($m_{A_H} < 120$ GeV) in the U-branch case or $m_h < 150$ GeV ($m_{A_H} < 120$ GeV) in the L-branch. Furthermore, these regions can be covered in AMS-02, even if $BF = 1$.

Finally, we show the 95% confidence level contour within the WMAP constraint

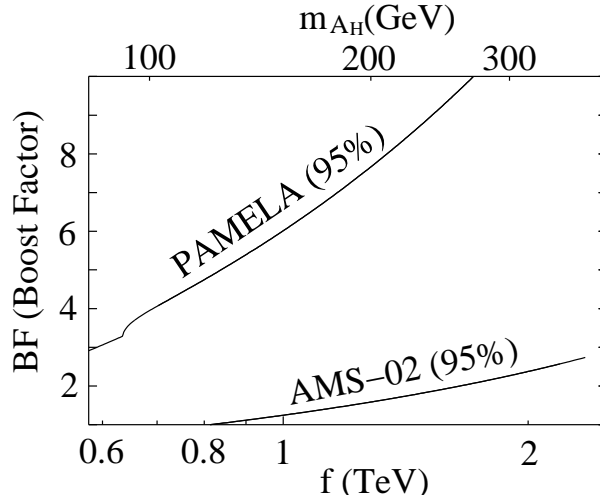


Figure 7: 95% confidence level for the statistical significance of the dark matter detection within the WMAP constraint in PAMELA and AMS-02 experiments. The region above the line can be distinguished from the background spectrum. The plot is depicted as a function of the breaking scale f (or the dark matter mass m_{A_H} on the top axis) and the boost factor BF . The lines for U- and L-branches coincide.

in $(f \text{ or } m_{A_H}, BF)$ -plane. The region above the line can be distinguished from the background in each experiment. Although both results in U- and L-branch cases are depicted in the figure, the contour lines are almost degenerate in this parameter space. In both branches, the annihilation modes are completely dominated by WW and ZZ bosons, and the positron production cross sections are the same once the WMAP constraint is applied. From the figure, we see that the signal may be detected in the PAMELA experiment when $f < 830 \text{ GeV}$ ($m_{A_H} < 120 \text{ GeV}$) and $BF > 5$. On the other hand, the AMS-02 experiment will cover a wide range of the parameter space including the region with $BF = 1$.

Here, we comment on the positron excess recently reported by HEAT collaboration [34]. In the measurement, the excess of high energy positrons ($1 \text{ GeV} < E < 30 \text{ GeV}$) has been observed. If the excess is due to the dark matter annihilation, its annihilation cross section should be large ($\sigma v \sim 10^{-24} \text{ cm}^3 \text{ sec}^{-1}$) unless the boost factor is large ($BF \sim 50-100$). Such large annihilation cross section is difficult to satisfy the WMAP constraint³. It is therefore unlikely that the excess observed at

³The cross section ($\sigma v \sim 2 \times 10^{-26} \text{ cm}^3 \text{ sec}^{-1}$) is required in order to explain WMAP result in the thermal relic scenario

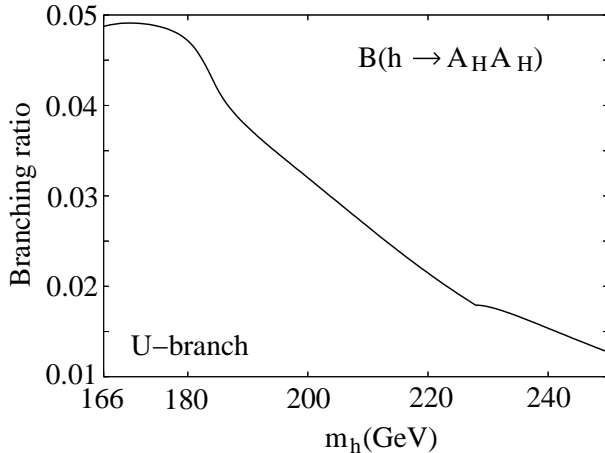


Figure 8: Branching ratio of the Higgs decay process into two dark matters along the center value of the U-branch as a function of the Higgs boson mass.

the HEAT experiment is explained by the signal of the dark matter in this model⁴.

V Summary and Discussions

We have studied the possibility to detect the dark matter in the littlest Higgs model with T-parity in future cosmic positron experiments. High energy positrons are produced from the dark matter annihilation through weak gauge boson decays. The resultant positron spectrum becomes hard, and the indirect detection of the dark matter is promising. We have performed the χ^2 -analysis to evaluate a confidence level to detect the dark matter signal in upcoming experiments. We have found that the signal will be detected in the PAMELA experiment, when the dark matter mass is less than 120 GeV and the boost factor is around 5 within the WMAP constraint. The region $m_{A_H} < 120$ GeV ($f < 830$ GeV) corresponds to $m_h < 300$ GeV in the U-branch, and $m_h < 150$ GeV in the L-branch. In the AMS-02 measurement, these regions can be covered even if there is no enhancement from the boost factor.

The positron spectrum in this model has a different feature compared to a bino-like neutralino dark matter in supersymmetric models. In the supersymmetric case, positrons are mostly produced from bottom quark decays, so that its spectrum becomes softer than the dark matter in the present model. Furthermore, the positron

⁴There are large uncertainties on the positron flux due to a solar modulation at GeV energy, which may be responsible to the HEAT excess [32].

production cross section is much smaller, because the bino-like dark matter annihilates in the p-wave. Therefore, the indirect detection of the dark matter in the littlest Higgs model with T-parity is easier than the supersymmetric case.

Finally, we discuss possible effects of the dark matter on the Higgs phenomenology. In the U-branch, the decay of a Higgs boson into a pair of the heavy photons contributes to the invisible width. The branching fraction of the process is shown in Fig.8 as a function of the Higgs boson mass. We see that the ratio is at a few percent level. Although this value seems to be beyond the currently estimated sensitivity to the total width measurement of the Higgs boson in LHC [35] and ILC [36], the measurement might be possible at a future muon collider [37].

We have concentrated on the positron signal of the dark matter in this paper. It is also interesting to consider other ways to search for the dark matter signals such as direct detection, and indirect detections using neutrinos, gamma-rays and anti-protons.

Acknowledgments

This work is supported in part by the Grant-in-Aid for Science Research, Ministry of Education, Science and Culture, Japan (No.16081211 for S.M and Y.O, No.15740164 for N.O., and Nos.13135225 and 17540286 for Y.O.).

Appendix Constraints from Electroweak Precision Measurements

In Appendix, we consider constraints on the Littlest Higgs model with T-parity from electroweak precision measurements. We follow the procedure in Ref.[12] using S, T and U parameters [38]. In that paper, it has been shown that main contributions to these parameters come from the top-sector in the model and custodial-symmetry violating effects from heavy gauge boson loops.

Contribution from the top-sector depends not only on the parameter f but also on a new parameter, $R \equiv \lambda_1/\lambda_2$. Using λ_1 and λ_2 , masses of the top quark and its T-even partner are given as $m_t = \lambda_1\lambda_2 v/(\lambda_1^2 + \lambda_2^2)^{1/2}$ and $m_{T^+} = (\lambda_1^2 + \lambda_2^2)^{1/2}f$. Instead of λ_1 , λ_2 , and f , we take m_t , R , and f as free parameters. We have calculated contributions from the top sector to the S, T and U parameters, and confirm the

results in Ref.[12], which are given by

$$\begin{aligned}
S_T &= \frac{1}{3\pi} \left(\frac{\lambda_1}{\lambda_2} \right)^2 \frac{m_t^2}{m_{T_+}^2} \left[-\frac{5}{2} + \log \frac{m_{T_+}^2}{m_t^2} \right], \\
T_T &= \frac{3}{8\pi} \frac{1}{s_W^2 c_W^2} \left(\frac{\lambda_1}{\lambda_2} \right)^2 \frac{m_t^4}{m_{T_+}^2 m_Z^2} \left[\log \frac{m_{T_+}^2}{m_t^2} - 1 + \frac{1}{2} \left(\frac{\lambda_1}{\lambda_2} \right)^2 \right], \\
U_T &= \frac{5}{6\pi} \left(\frac{\lambda_1}{\lambda_2} \right)^2 \frac{m_t^2}{m_{T_+}^2}.
\end{aligned} \tag{25}$$

We have also calculated contributions from heavy gauge boson loops in the general R_ξ gauge. We have obtained ξ independent results. Final expression, however, is not consistent with the result in Ref.[12], in which the Landau gauge has been used. Detail of our calculation is presented in the followings.

In order to define the R_ξ gauge, we first consider the mixing term between gauge bosons and derivatives of Nambu-Goldstone (NG) bosons up to appropriate order of v/f . The non-linear sigma field Σ is expanded by the NG fields as

$$\begin{aligned}
\Sigma &\equiv \exp [2i(\langle \Pi \rangle + \delta \Pi)/f] \Sigma_0 \\
&= (\text{constant}) + (\text{terms} \propto \delta \Pi) + (\text{terms} \propto \delta \Pi^2) + \dots,
\end{aligned} \tag{26}$$

where

$$\begin{aligned}
\langle \Pi \rangle &= \begin{pmatrix} 0 & 0 & 0 & 0 & 0 \\ 0 & 0 & v/2 & 0 & 0 \\ 0 & v/2 & 0 & 0 & v/2 \\ 0 & 0 & 0 & 0 & 0 \\ 0 & 0 & v/2 & 0 & 0 \end{pmatrix}, \\
\delta \Pi &= \begin{pmatrix} -\frac{\omega^0}{2} - \frac{\eta}{\sqrt{20}} & -\frac{\omega^\dagger}{\sqrt{2}} & -\frac{i\pi^\dagger}{\sqrt{2}} & -i\phi^{++} & -\frac{i\phi^\dagger}{\sqrt{2}} \\ -\frac{\omega}{\sqrt{2}} & \frac{\omega^0}{2} - \frac{\eta}{\sqrt{20}} & \frac{h+i\pi^0}{2} & -\frac{i\phi^\dagger}{\sqrt{2}} & \frac{-i\phi^0+\phi_P^0}{\sqrt{2}} \\ \frac{i\pi}{\sqrt{2}} & \frac{h-i\pi^0}{2} & \frac{2\eta}{\sqrt{5}} & -\frac{i\pi^\dagger}{\sqrt{2}} & \frac{h+i\pi^0}{2} \\ i\phi^{--} & \frac{i\phi}{\sqrt{2}} & \frac{i\pi}{\sqrt{2}} & -\frac{\omega^0}{2} - \frac{\eta}{\sqrt{20}} & -\frac{\omega}{\sqrt{2}} \\ \frac{i\phi}{\sqrt{2}} & \frac{i\phi^0+\phi_P^0}{\sqrt{2}} & \frac{h-i\pi^0}{2} & -\frac{\omega^\dagger}{\sqrt{2}} & \frac{\omega^0}{2} - \frac{\eta}{\sqrt{20}} \end{pmatrix}.
\end{aligned} \tag{27}$$

We used the notation adopted in Ref.[12] for the NG fields in the $\delta \Pi$ matrix. It is well known that the constant term is obtained in an exact manner as

$$(\text{constant}) = \begin{pmatrix} 0 & 0 & 0 & 1 & 0 \\ 0 & -(1-c)/2 & is/\sqrt{2} & 0 & (1+c)/2 \\ 0 & is/\sqrt{2} & c & 0 & is/\sqrt{2} \\ 1 & 0 & 0 & 0 & 0 \\ 0 & (1+c)/2 & is/\sqrt{2} & 0 & -(1-c)/2 \end{pmatrix}, \tag{28}$$

where $s = \sin(\sqrt{2}v/f)$, $c = \cos(\sqrt{2}v/f)$. Thanks to the Feynman formula [39], we can also derive terms proportional to $\delta\Pi$ exactly as follows,

$$(\text{terms} \propto \delta\Pi) = \int_0^1 d\alpha e^{2i(1-\alpha)\langle\Pi\rangle/f} \left(\frac{2\delta\Pi i}{f} \right) e^{2i\alpha\langle\Pi\rangle/f} \Sigma_0. \quad (29)$$

The integration by the parameter α can be exactly performed. Due to the complex form of the result, we omit to write it down. Using these exact expressions in Eqs.(28) and (29), the mixing term induced from the kinetic term in Eq.(3) is written as

$$\begin{aligned} & \frac{gf^2(1-c)}{2v} W^a \partial\pi^a + \left(\frac{gf^2}{2} W_H \cdot \left[\left(\frac{1}{f} + \frac{s}{\sqrt{2}v} \right) \partial\omega^\dagger - i \left(\frac{1}{f} - \frac{s}{\sqrt{2}v} \right) \partial\phi^\dagger \right] + h.c. \right) \\ & + \frac{gf^2}{8} Z_H \cdot \left[\left(\frac{7}{f} + \frac{sc}{\sqrt{2}v} \right) \partial\omega^0 - \sqrt{2} \left(\frac{1}{f} - \frac{sc}{\sqrt{2}v} \right) \partial\phi_P^0 + \sqrt{5} \left(\frac{1}{f} - \frac{sc}{\sqrt{2}v} \right) \partial\eta \right], \end{aligned} \quad (30)$$

where $W_H = (W_H^1 + iW_H^2)/\sqrt{2}$, and $Z_H = W_H^3$. We neglect the effect of U(1) gauge interactions for simplicity ($g' = 0$).

Due to the electroweak symmetry breaking, the NG mode absorbed in the longitudinal component of the heavy gauge boson W_H (Z_H) is given by the combination of ω and ϕ (ω^0 , ϕ_P^0 , and η). Thus, ‘‘would-be NG’’ modes are written as

$$\begin{aligned} \tilde{\pi}^a &= N_{\tilde{\pi}} \pi^a, \\ \tilde{\omega} &= N_{\tilde{\omega}} \left[\left(1 + \frac{fs}{\sqrt{2}v} \right) \omega + i \left(1 - \frac{fs}{\sqrt{2}v} \right) \phi \right], \\ \tilde{\omega}^0 &= N_{\tilde{\omega}^0} \left[\left(7 + \frac{fsc}{\sqrt{2}v} \right) \omega^0 - \sqrt{2} \left(1 - \frac{fsc}{\sqrt{2}v} \right) \phi_P^0 + \sqrt{5} \left(1 - \frac{fsc}{\sqrt{2}v} \right) \eta \right]. \end{aligned} \quad (31)$$

Note that these modes become π^a , ω , and ω^0 at the leading order of v/f . Normalization constants, N_x ($x = \tilde{\pi}$, $\tilde{\omega}$, and $\tilde{\omega}^0$), are determined by considering kinetic terms of NG bosons. The kinetic terms are also obtained exactly as

$$\begin{aligned} & \frac{f^2(1-c)}{2v^2} (\partial\pi^a)^2 + \frac{1}{2} (\partial h)^2 + \partial\phi^{++} \partial\phi^{--} + \frac{f^2(1-c)}{2v^2} (\partial\phi^0)^2 \\ & + \left(\frac{(1-c)f^2}{2v^2} + \frac{1}{2} \right) (\partial\phi^\dagger \partial\phi + \partial\omega^\dagger \partial\omega) + i \left(\frac{(1-c)f^2}{2v^2} - \frac{1}{2} \right) (\partial\phi^\dagger \partial\omega - \partial\omega^\dagger \partial\phi) \\ & + \frac{1}{16} \left(7 + \frac{s^2 f^2}{2v^2} \right) (\partial\omega^0)^2 + \frac{1}{16} \left(3 + \frac{5s^2 f^2}{2v^2} \right) (\partial\eta)^2 + \frac{1}{8} \left(3 + \frac{s^2 f^2}{2v^2} \right) (\partial\phi_P^0)^2 \\ & + \frac{\sqrt{5}}{8} \left(1 - \frac{s^2 f^2}{2v^2} \right) \partial\omega^0 \partial\eta - \frac{\sqrt{2}}{8} \left(1 - \frac{s^2 f^2}{2v^2} \right) \partial\omega^0 \partial\phi_P^0 + \frac{\sqrt{10}}{8} \left(1 - \frac{s^2 f^2}{2v^2} \right) \partial\eta \partial\phi_P^0. \end{aligned} \quad (32)$$

As seen from the equation, we find that kinetic terms of π , ω , ϕ , ω^0 , ϕ_P^0 , η , and ϕ^0 are not canonically normalized due to the electroweak symmetry breaking. Therefore,

we have to redefine these NG fields by normalized ones. After the redefinition, we found the normalization constants, N_x , in Eq.(31) are given as

$$N_{\tilde{\pi}} = \frac{f\sqrt{1-c}}{v}, \quad N_{\tilde{\omega}} = \frac{1}{\sqrt{3+c}}, \quad N_{\tilde{\omega}^0} = \frac{1}{2\sqrt{14+2c^2}}. \quad (33)$$

Once we obtain canonically normalized ‘‘would-be NG’’ modes, we can determine gauge fixing functions to cancel the mixing term in Eq.(30). Those functions are

$$G^a = \frac{1}{\sqrt{\xi}} \left[\partial W^a - \xi \frac{gf\sqrt{1-c}}{2} \tilde{\pi}^a \right], \quad (34)$$

$$G_H^{1,2} = \frac{1}{\sqrt{\xi}} \left[\partial W_H^a - \xi \frac{gf\sqrt{3+c}}{2} \tilde{\omega}^a \right], \quad G_H^3 = \frac{1}{\sqrt{\xi}} \left[\partial Z_H - \xi \frac{gf\sqrt{7+c^2}}{2\sqrt{2}} \tilde{\omega}^0 \right].$$

Using these functions, mass terms of the ‘‘would-be NG’’ modes turn out to be

$$\left. \frac{(G^a)^2 + (G_H^a)^2}{2} \right|_{\text{NG mass}} = \frac{\xi}{2} m_W^2 (\tilde{\pi}^a)^2 + \xi m_{W_H}^2 \tilde{\omega}^\dagger \tilde{\omega} + \frac{\xi}{2} (m_{W_H}^2 + \Delta M^2) (\tilde{\omega}^0)^2, \quad (35)$$

where $m_W^2 = g^2 f^2 (1-c)/4$, $m_{W_H}^2 = g^2 f^2 (3+c)/4$, and $\Delta M^2 = g^2 f^2 (1-c)^2/8$. Hence, with $\xi = 1$, ‘‘would-be NG’’ masses coincide with those of corresponding gauge bosons at any order of v/f .

We are now in position to calculate the contribution to the T parameter from heavy gauge boson loops. With expressions of ‘‘would-be NG’’ modes in Eq.(31), interactions relevant to the calculation are given as follows,

$$\mathcal{L} = \mathcal{L}_{V_L V_H V_H} + \mathcal{L}_{V_L V_L V_H V_H} + \mathcal{L}_{\text{Ghost}} + \mathcal{L}_{V_L \text{NGNG}} + \mathcal{L}_{V_L V_L \text{NGNG}} + \mathcal{L}_{V_L V_H \text{NG}},$$

$$\begin{aligned} \mathcal{L}_{V_L V_H V_H} = & ig \left[Z_\mu W_{H\nu}^\dagger (\partial^\mu W_H^\nu - \partial^\nu W_H^\mu) - Z_\mu W_{H\nu} (\partial^\mu W_H^{\dagger\nu} - \partial^\nu W_H^{\dagger\mu}) \right. \\ & + \partial_\mu Z_\nu (W_H^{\dagger\mu} W_H^\nu - W_H^\mu W_H^{\dagger\nu}) + W_\mu^\dagger W_{H\nu} (\partial^\mu Z_H^\nu - \partial^\nu Z_H^\mu) \\ & - W_\mu^\dagger Z_{H\nu} (\partial^\mu W_H^\nu - \partial^\nu W_H^\mu) + \partial_\mu W_\nu^\dagger (Z_H^\nu W_H^\mu - Z_H^\mu W_H^\nu) \\ & - W_\mu W_{H\nu}^\dagger (\partial^\mu Z_H^\nu - \partial^\nu Z_H^\mu) + W_\mu Z_{H\nu} (\partial^\mu W_H^{\dagger\nu} - \partial^\nu W_H^{\dagger\mu}) \\ & \left. - \partial_\mu W_\nu (Z_H^\nu W_H^{\dagger\mu} - Z_H^\mu W_H^{\dagger\nu}) \right], \quad (36) \end{aligned}$$

$$\begin{aligned} \mathcal{L}_{V_L V_L V_H V_H} = & -\frac{g^2}{2} \left[f^{abe} f^{cde} g^{\mu\mu'} g^{\nu\nu'} + f^{ade} f^{cbe} g^{\mu\mu'} g^{\nu\nu'} + f^{ace} f^{bde} g^{\mu\nu} g^{\mu'\nu'} \right] \\ & \times W_\mu^a W_\nu^b W_{H\mu'}^c W_{H\nu'}^d, \quad (37) \end{aligned}$$

$$\mathcal{L}_{\text{Ghost}} = gf^{abc} \bar{\eta}_H^a \partial^\mu (W_\mu^b \eta_H^c), \quad (38)$$

$$\begin{aligned}
\mathcal{L}_{\text{VLNGNG}} &= \frac{g}{2} \left[\frac{3c+5}{c+3} Z \cdot (\tilde{\omega} i \partial \tilde{\omega}^\dagger - \tilde{\omega}^\dagger i \partial \tilde{\omega}) \right. \\
&\quad \left. + \frac{c^2+4c+11}{\sqrt{2(c+3)(c^2+7)}} \{W \cdot (\tilde{\omega}^\dagger i \partial \tilde{\omega}^0 - \tilde{\omega}^0 i \partial \tilde{\omega}^\dagger) + h.c.\} \right] \quad (39) \\
&= g \left(1 - \frac{v^2}{8f^2} - \frac{v^4}{96f^4} \right) \left[Z \cdot (\tilde{\omega} i \partial \tilde{\omega}^\dagger - \tilde{\omega}^\dagger i \partial \tilde{\omega}) \right. \\
&\quad \left. + \{W \cdot (\tilde{\omega}^\dagger i \partial \tilde{\omega}^0 - \tilde{\omega}^0 i \partial \tilde{\omega}^\dagger) + h.c.\} \right] + \mathcal{O} \left(\frac{v^6}{f^6} \right),
\end{aligned}$$

$$\begin{aligned}
\mathcal{L}_{\text{VLVLNGNG}} &= g^2 \left[C_{\tilde{\omega}^0 \tilde{\omega}^0 Z Z} (\tilde{\omega}^0)^2 Z_\mu Z^\mu + C_{\tilde{\omega}^\dagger \tilde{\omega} Z Z} \tilde{\omega}^\dagger \tilde{\omega} Z_\mu Z^\mu \right. \\
&\quad \left. + C_{\tilde{\omega}^\dagger \tilde{\omega} W^\dagger W} \tilde{\omega}^\dagger \tilde{\omega} W_\mu^\dagger W^\mu + C_{\tilde{\omega}^0 \tilde{\omega}^0 W^\dagger W} (\tilde{\omega}^0)^2 W_\mu^\dagger W^\mu \right], \quad (40)
\end{aligned}$$

$$\begin{aligned}
\mathcal{L}_{\text{VLVHNG}} &= ig^2 f \left[\frac{\sqrt{2}(1+c)}{\sqrt{c^2+7}} \tilde{\omega}^0 W_\mu^\dagger W_H^\mu + \frac{c^2+2c+5}{4\sqrt{c+3}} \tilde{\omega}^\dagger W_\mu Z_H^\mu \right. \\
&\quad \left. + \frac{1+c}{\sqrt{c+3}} \tilde{\omega} W_{H\mu}^\dagger Z^\mu \right] + h.c. \\
&= ig^2 f \left[\left(1 - \frac{3v^2}{8f^2} - \frac{5v^4}{128f^4} \right) \tilde{\omega}^0 W_\mu^\dagger W_H^\mu + \left(1 - \frac{3v^2}{8f^2} + \frac{19v^4}{128f^4} \right) \tilde{\omega}^\dagger W_\mu Z_H^\mu \right. \\
&\quad \left. + \left(1 - \frac{3v^2}{8f^2} + \frac{3v^4}{128f^4} \right) \tilde{\omega} W_{H\mu}^\dagger Z^\mu \right] + h.c. + \mathcal{O} \left(\frac{v^6}{f^6} \right). \quad (41)
\end{aligned}$$

In order to calculate the coefficients, C, in Eq.(40), we need not only the linear terms in Eq.(29), but also those proportional to $\delta\Pi^2$. Since it is difficult to obtain the $\delta\Pi^2$ terms in an exact manner, we have calculated these terms with the expansion of v/f . Up to the order of $(v/f)^6$, the coefficients turn out to be

$$\begin{aligned}
C_{\tilde{\omega}^0 \tilde{\omega}^0 Z Z} &= -\frac{v^2}{96f^2} + \frac{37v^4}{5760f^4} + \mathcal{O} \left(\frac{v^6}{f^6} \right), \\
C_{\tilde{\omega}^\dagger \tilde{\omega} Z Z} &= 1 - \frac{13v^2}{48f^2} - \frac{47v^4}{2880f^4} + \mathcal{O} \left(\frac{v^6}{f^6} \right), \\
C_{\tilde{\omega}^\dagger \tilde{\omega} W^\dagger W} &= 1 - \frac{7v^2}{24f^2} + \frac{163v^4}{1440f^4} + \mathcal{O} \left(\frac{v^6}{f^6} \right), \\
C_{\tilde{\omega}^0 \tilde{\omega}^0 W^\dagger W} &= 1 - \frac{13v^2}{48f^2} - \frac{383v^4}{2880f^4} + \mathcal{O} \left(\frac{v^6}{f^6} \right). \quad (42)
\end{aligned}$$

Interactions in $\mathcal{L}_{\text{VLVH}}^{\text{VH}}$ and $\mathcal{L}_{\text{VLVL}}^{\text{VH}}^{\text{VH}}$ are gauge self-interactions coming from gauge kinetic terms, while ghost interactions in $\mathcal{L}_{\text{Ghost}}$ are derived from the gauge fixing functions in Eq.(34). Interactions in $\mathcal{L}_{\text{VLNGNG}}$, $\mathcal{L}_{\text{VLVLNGNG}}$ and $\mathcal{L}_{\text{VLVHNG}}$ have been obtained by expanding the kinetic term in Eq.(3) in terms of NG fields.

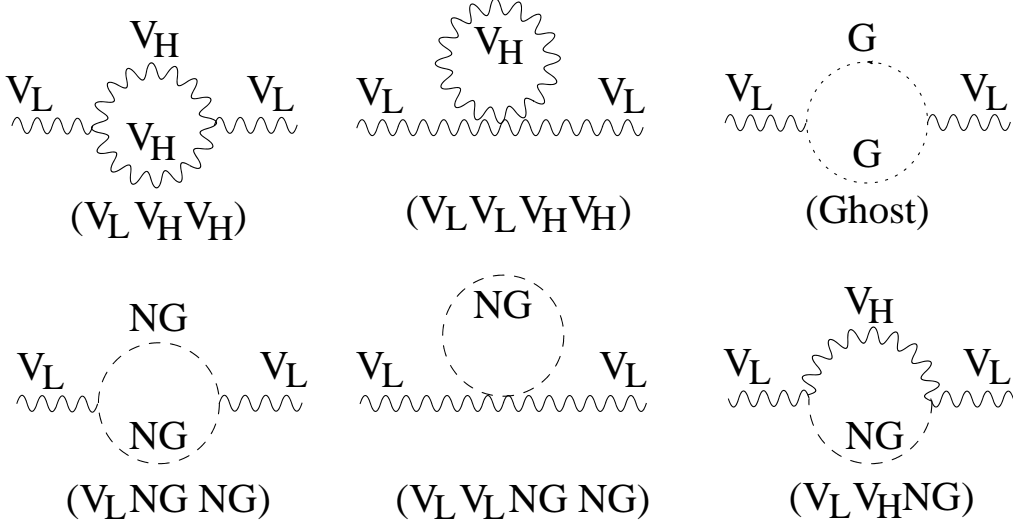


Figure 9: Heavy gauge boson loop diagrams contributing to the T parameter.

There are six kinds of loop diagrams involving heavy gauge and NG bosons contributing to the T parameter as shown in Fig.9. Those are diagrams with three points gauge self-interactions ($V_L V_H V_H$), four points gauge self-interactions ($V_L V_L V_H V_H$), ghost interactions (Ghost), three points NG gauge interactions ($V_L NG NG$), four points NG gauge interactions ($V_L V_L NG NG$), and interactions in $\mathcal{L}_{V_L V_H NG}$ ($V_L V_H NG$). In all diagrams except the last one, the contributions to the T parameter come from the mass difference between W_H and Z_H . In the last diagram, difference among coefficients in Eq.(41) is the source of the T parameter.

The leading logarithmic divergent contribution from each diagram is

$$\begin{aligned}
T(V_L V_H V_H) &= \frac{4\pi}{s_W^2 c_W^2 m_Z^2} \left(\frac{\Delta M^2}{16\pi^2} \right) \left(3 + \frac{3}{4}\xi + \frac{3}{4}\xi^2 \right) \ln \left(\frac{\Lambda^2}{m_{W_H}^2} \right), \\
T(V_L V_L V_H V_H) &= \frac{4\pi}{s_W^2 c_W^2 m_Z^2} \left(\frac{\Delta M^2}{16\pi^2} \right) \left(-\frac{9}{4} - \frac{3}{4}\xi^2 \right) \ln \left(\frac{\Lambda^2}{m_{W_H}^2} \right), \\
T(\text{Ghost}) &= \frac{4\pi}{s_W^2 c_W^2 m_Z^2} \left(\frac{\Delta M^2}{16\pi^2} \right) \left(-\frac{1}{2}\xi \right) \ln \left(\frac{\Lambda^2}{m_{W_H}^2} \right), \\
T(V_L NG NG) &= \frac{4\pi}{s_W^2 c_W^2 m_Z^2} \left(\frac{\Delta M^2}{16\pi^2} \right) (+\xi) \ln \left(\frac{\Lambda^2}{m_{W_H}^2} \right), \\
T(V_L V_L NG NG) &= \frac{4\pi}{s_W^2 c_W^2 m_Z^2} \left(\frac{\Delta M^2}{16\pi^2} \right) (-\xi) \ln \left(\frac{\Lambda^2}{m_{W_H}^2} \right), \\
T(V_L V_H NG) &= \frac{4\pi}{s_W^2 c_W^2 m_Z^2} \left(\frac{\Delta M^2}{16\pi^2} \right) \left(-\frac{3}{4} - \frac{1}{4}\xi \right) \ln \left(\frac{\Lambda^2}{m_{W_H}^2} \right). \quad (43)
\end{aligned}$$

After summing all contributions, we have found that the logarithmic divergent cor-

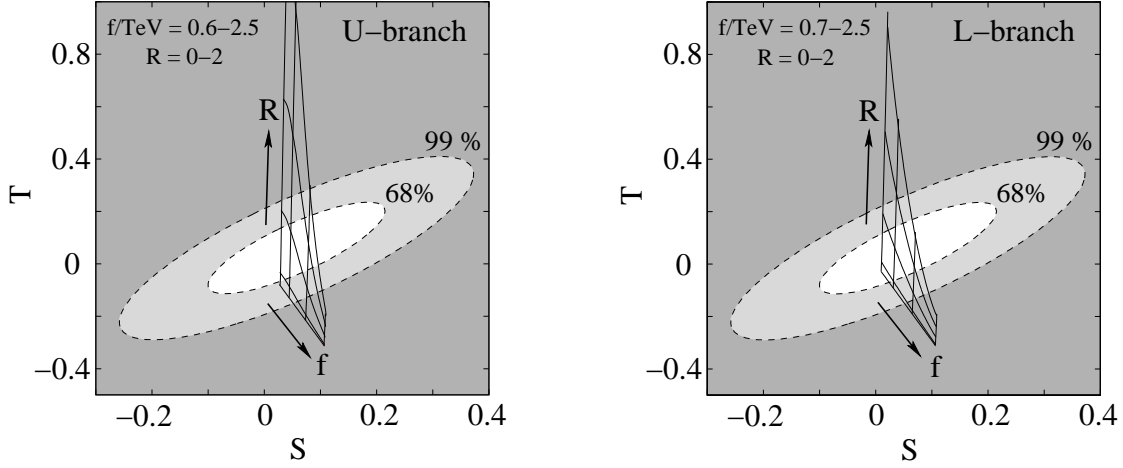


Figure 10: Contributions to S and T parameters in the Littlest Higgs model with T-parity (solid lines) for $0 < R < 2$ and f along the center value of the U-branch (left figure) and L-branch (right figure). From bottom to top, lines correspond to $R = 0, 0.5, 1, 1.5$ and 2 . From left to right, f corresponds to the point I, II, III, and VII for U-branch, IV, V, VI, and VII for L-branch in Fig.3. Constraints on S and T parameters from electroweak precision measurements are also shown at 68% and 99% confidence level. The plot assumes $U = 0$.

rection is completely canceled,

$$T_{V_H} = 0 \times \frac{4\pi}{s_W^2 c_W^2 m_Z^2} \left(\frac{\Delta M^2}{16\pi^2} \right) \ln \left(\frac{\Lambda^2}{m_{W_H}^2} \right) + (\text{finite terms}) . \quad (44)$$

This result differs from Eq.(3.6) in Ref.[12]. Therefore, the contribution to the T parameter at this order of v/f comes from a finite term.

In addition to the loop contribution, we expect that the following operator can arise at the cutoff scale [12],

$$\mathcal{L}_c = \delta_c \frac{g^2}{16\pi^2} f^2 \text{Tr} [(Q_i^a D_\mu \Sigma)(Q_i^a D^\mu \Sigma)^*] , \quad (45)$$

which gives the contribution to the T parameter at the same order of the finite term,

$$T(\text{Cutoff}) = \frac{4\pi}{s_W^2 c_W^2 m_Z^2} \left(\frac{\Delta M^2}{16\pi^2} \right) (-\delta_c) . \quad (46)$$

The value of δ_c is determined by the UV-completion of the Littlest Higgs model with T-parity, and it is naturally expected to be $\mathcal{O}(1)$. By comparing the contribution from the top sector with those from heavy gauge boson loops and the cutoff scale

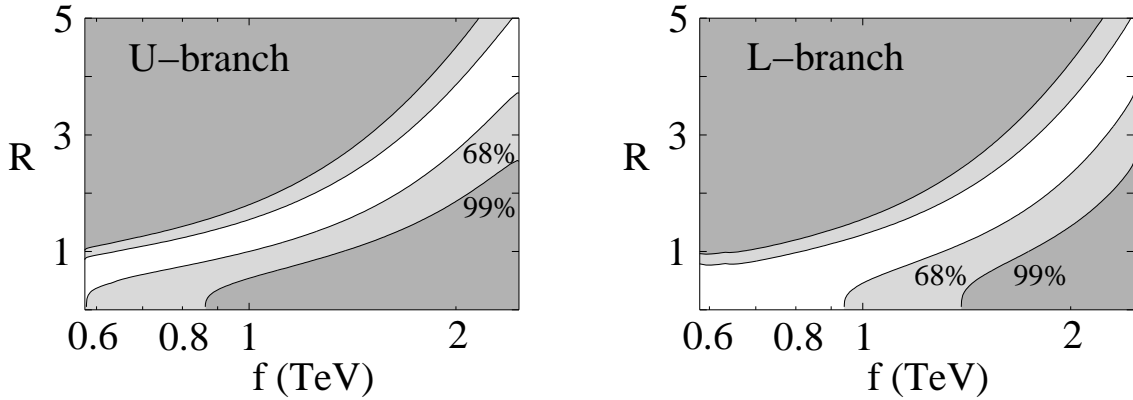


Figure 11: Constraints on the model parameters, R and f , at 68% and 99% confidence level. At each point in these figures, the Higgs mass is determined to satisfy the WMAP constraint on the U-branch (left figure) and L-branch (right figure).

operator, the latter contributions turns out to be small as long as the finite term in Eq.(44) does not have a large coefficient. In fact, $T(\text{Cutoff})$ in Eq.(46) is 8% of T_T in Eq.(25), when we take $f = 1$ TeV, $R = 1$, and $\delta_c = 1$. Therefore, we neglect these contributions to derive electroweak precision constraints on the model.

The contributions to S and T parameters from the Littlest Higgs model with T-parity are depicted in Fig.10. Constraints on S and T parameters from electroweak precision measurements at 68% and 99% confidence level are also shown. Solid lines are predictions of the model for $0 < R < 2$ and f along the center value of the U-branch (left figure) and L-branch (right figure). For depicting contours of the constraints from the measurements, we have used three experimental values following papers [40], W boson mass ($m_W = 80.412 \pm 0.042$ GeV), weak mixing angle ($\sin^2 \theta_{eff}^{lept} = 0.23153 \pm 0.00016$), and leptonic width of the Z boson ($\Gamma_l = 83.985 \pm 0.086$ MeV) [41]. We have also used values of the fine structure constant on the Z pole ($\alpha^{-1}(m_Z) = 128.950 \pm 0.048$) and the top quark mass ($m_t = 172.7 \pm 2.9$ GeV) [42]. The origin of the S-T plane is fixed by using the reference Higgs mass, $m_h = 100$ GeV. In this figure, we can see that, even for a large value of f , there is a parameter region consistent with the electroweak precision measurements with appropriate choice of R . In the case of large f , the Higgs boson becomes heavy and gives large contributions to the S and T parameters. These contributions, however, can be canceled by those from the top loops (t and T_+) due to the large mixing angle ($R > 1$).

In Fig.11, constraints for the model parameters, R and f , are shown at 68% and

99% confidence level. At each point in these figures, the Higgs mass is determined to satisfy the WMAP constraint on the U-branch (left figure) and L-branch (right figure). Possible range of R can be determined by requiring λ_1 and λ_2 couplings to be within the perturbative range, which results in $0.2 \lesssim R \lesssim 5$. As seen in these figures, the entire allowed region can be consistent with the electroweak precision measurements.

References

- [1] R. Barbieri and A. Strumia, Phys. Lett. B **433** (1998) 63; R. Barbieri and A. Strumia, arXiv:hep-ph/0007265.
- [2] N. Arkani-Hamed, A. G. Cohen and H. Georgi, Phys. Lett. B **513** (2001) 232; N. Arkani-Hamed, A. G. Cohen, E. Katz, A. E. Nelson, T. Gregoire and J. G. Wacker, JHEP **0208** (2002) 021.
- [3] N. Arkani-Hamed, A. G. Cohen, E. Katz and A. E. Nelson, JHEP **0207** (2002) 034.
- [4] C. Csaki, J. Hubisz, G. D. Kribs, P. Meade and J. Terning, Phys. Rev. D **67** (2003) 115002; J. L. Hewett, F. J. Petriello and T. G. Rizzo, JHEP **0310** (2003) 062; C. Csaki, J. Hubisz, G. D. Kribs, P. Meade and J. Terning, Phys. Rev. D **68** (2003) 035009; T. Gregoire, D. R. Smith and J. G. Wacker, Phys. Rev. D **69** (2004) 115008; M. C. Chen and S. Dawson, Phys. Rev. D **70** (2004) 015003; Z. Han and W. Skiba, Phys. Rev. D **72** (2005) 035005; W. Kilian and J. Reuter, Phys. Rev. D **70** (2004) 015004.
- [5] H. C. Cheng and I. Low, JHEP **0309** (2003) 051.
- [6] H. C. Cheng and I. Low, JHEP **0408** (2004) 061.
- [7] I. Low, JHEP **0410** (2004) 067.
- [8] D. N. Spergel *et al.* [WMAP Collaboration], Astrophys. J. Suppl. **148** (2003) 175; C. L. Bennett *et al.*, Astrophys. J. Suppl. **148** (2003) 1.
- [9] For reviews,
 G. Jungman, M. Kamionkowski and K. Griest, Phys. Rept. **267** (1996) 195;
 L. Bergstrom, Rept. Prog. Phys. **63**, (2000) 793; G. Bertone, D. Hooper and J. Silk, Phys. Rept. **405** (2005) 279; C. Munoz, Int. J. Mod. Phys. A **19** (2004) 3093.

- [10] J. R. Primack, Nucl. Phys. Proc. Suppl. **124** (2003) 3.
- [11] J. Hubisz and P. Meade, Phys. Rev. D **71** (2005) 035016, (For the correct paramter region consistent with the WMAP observation, see the figure in the revised vergion, hep-ph/0411264v3).
- [12] J. Hubisz, P. Meade, A. Noble and M. Perelstein, JHEP **0601** (2006) 135.
- [13] S. Rudaz and F. W. Stecker, Astrophys. J. **325** (1988) 16; J. R. Ellis, R. A. Flores, K. Freese, S. Ritz, D. Seckel and J. Silk, Phys. Lett. B **214** (1988) 403; A. J. Tylka, Phys. Rev. Lett., **63** (1989) 840; M. S. Turner and F. Wilczek, Phys. Rev. D, **42** (1990) 1001; A. J. Tylka, Phys. Rev. D **43** (1991) 1774.
- [14] E. A. Baltz, J. Edsjo, K. Freese and P. Gondolo, arXiv:astro-ph/0211239; G. L. Kane, L. T. Wang and T. T. Wang, Phys. Lett. B **536** (2002) 263; W. de Boer, C. Sander, M. Horn and D. Kazakov, Nucl. Phys. Proc. Suppl. **113** (2002) 221; G. L. Kane, L. T. Wang and J. D. Wells, Phys. Rev. D **65** (2002) 057701; E. A. Baltz, J. Edsjo, K. Freese and P. Gondolo, Phys. Rev. D **65** (2002) 063511; D. Hooper and G. D. Kribs, Phys. Rev. D **70** (2004) 115004; S. Profumo and P. Ullio, JCAP **0407** (2004) 006.
- [15] E. A. Baltz and J. Edsjo, Phys. Rev. D **59** (1999) 023511.
- [16] D. Hooper and J. Silk, Phys. Rev. D **71** (2005) 083503.
- [17] J. Silk and M. Srednicki, Phys. Rev. Lett. **53** (1984) 624; S. Rudaz and F. W. Stecker, Astrophys. J. 325 (1988) 16; A. Bottino, F. Donato, N. Fornengo and P. Salati, Phys. Rev. D **58** (1998) 123503; L. Bergstrom, J. Edsjo and P. Ullio, arXiv:astro-ph/9906034; F. Donato, N. Fornengo, D. Maurin, P. Salati and R. Taillet, Phys. Rev. D **69** (2004) 063501.
- [18] M. Circella [PAMELA Collaboration], Nucl. Instrum. Meth. A **518** (2004) 153; P. Spillantini, Nucl. Instrum. Meth. B **214** (2004) 116.
- [19] F. Barao [AMS-02 Collaboration], Nucl. Instrum. Meth. A **535** (2004) 134.
- [20] M. Schmaltz and D. Tucker-Smith, arXiv:hep-ph/0502182; M. Perelstein, arXiv:hep-ph/0512128.
- [21] G. Burdman, M. Perelstein and A. Pierce, Phys. Rev. Lett. **90** (2003) 241802 [Erratum-ibid. **92** (2004) 049903]; T. Han, H. E. Logan, B. McElrath and L. T. Wang, Phys. Rev. D **67** (2003) 095004; M. Perelstein, M. E. Peskin and A. Pierce, Phys. Rev. D **69** (2004) 075002.

- [22] A. Birkedal, A. Noble, M. Perelstein and A. Spray, arXiv:hep-ph/0603077.
- [23] E. W. Kolb and M. S. Turner, *The Early Universe*, (Addison-Wesley, Reading, MA, 1990).
- [24] J. F. Navarro, C. S. Frenk and S. D. M. White, *Astrophys. J.* **462** (1996) 563; J. F. Navarro, C. S. Frenk and S. D. M. White, *Astrophys. J.* **490** (1997) 493; B. Moore, S. Ghigna, F. Governato, G. Lake, T. Quinn, J. Stadel and P. Tozzi, *Astrophys. J.* **524** (1999) L19; J. Diemand, B. Moore and J. Stadel, *Mon. Not. Roy. Astron. Soc.* **353** (2004) 624.
- [25] G. Corcella *et al.*, interfering gluons (including supersymmetric processes),” *JHEP* **0101** (2001) 010.
- [26] J. Hisano, S. Matsumoto, O. Saito and M. Senami, arXiv:hep-ph/0511118.
- [27] J. Silk and A. Stebbins, *Astrophys. J.* **411** (1993) 439; L. Bergstrom, J. Edsjo and P. Gondolo, *Phys. Rev. D* **59** (1999) 043506.
- [28] V. Berezhinsky, V. Dokuchaev and Y. Eroshenko, *Phys. Rev. D* **68** (2003) 103003.
- [29] A. W. Strong and I. V. Moskalenko, *Astrophys. J.* **509** (1998) 212; I. V. Moskalenko and A. W. Strong, *Phys. Rev. D* **60** (1999) 063003; D. Maurin, F. Donato, R. Taillet and P. Salati, *Astrophys. J.* **555** (2001) 585; D. Maurin, R. Taillet and F. Donato, *Astron. Astrophys.* **394** (2002) 1039; I. V. Moskalenko, A. W. Strong, S. G. Mashnik and J. F. Ormes, *Astrophys. J.* **586** (2003) 1050; D. Hooper, J. E. Taylor and J. Silk, *Phys. Rev. D* **69** (2004) 103509.
- [30] M. S. Longair, *High-energy astrophysics. Vol. 2* Cambridge University Press, New York, 1994.
- [31] A. Barrau, G. Boudoul, F. Donato, D. Maurin, P. Salati and R. Taillet, *Astron. Astrophys.* **388** (2002) 676.
- [32] L. J. Gleeson and W. I. Axford, *Astrophys. J.* **149** (1967) L115.
- [33] I. V. Moskalenko and A. W. Strong, *Astrophys. J.* **493** (1998) 694.
- [34] S. W. Barwick *et al.* [HEAT Collaboration], *Phys. Rev. Lett.* **75** (1995) 390. S. W. Barwick *et al.* [HEAT Collaboration], *Astrophys. J.* **482** (1997) L191;
- [35] V. Drollinger and A. Sopczak, *Eur. Phys. J. directC* **3** (2001) N1.
- [36] N. Meyer and K. Desch, *Eur. Phys. J. C* **35** (2004) 171.
- [37] M. M. Alsharoa *et al.* [Muon Collider/Neutrino Factory Collaboration], *Phys. Rev. ST Accel. Beams* **6** (2003) 081001.

- [38] M. E. Peskin and T. Takeuchi, Phys. Rev. D **46** (1992) 381.
- [39] See, for example, p.12, Yuri Makeenko, “*Method of Contemporary Gauge Theory*” (Cambridge university press).
- [40] W. J. Marciano, arXiv:hep-ph/0003181; M. Perelstein, M. E. Peskin and A. Pierce, Phys. Rev. D **69** (2004) 075002.
- [41] [ALEPH Collaboration], Phys. Rept. **427** (2006) 257.
- [42] [CDF Collaboration], arXiv:hep-ex/0507091.